

Transient Solid-State Laser Activation of Indium for High-Performance Reduction of CO₂ to Formate

Weihua Guo, Yuefeng Zhang, Jianjun Su, Yun Song, Libei Huang, Le Cheng, Xiaohu Cao, Yubing Dou, Yangbo Ma, Chenyan Ma, He Zhu, Tingting Zheng, Zhaoyu Wang, Hao Li, Zhanxi Fan, Qi Liu, Zhiyuan Zeng,* Juncai Dong, Chuan Xia, Ben Zhong Tang, and Ruquan Ye*

Deficiencies in understanding the local environment of active sites and limited synthetic skills challenge the delivery of industrially-relevant current densities with low overpotentials and high selectivity for CO₂ reduction. Here, a transient laser induction of metal salts can stimulate extreme conditions and rapid kinetics to produce defect-rich indium nanoparticles (L-In) is reported. Atomic-resolution microscopy and X-ray absorption disclose the highly defective and undercoordinated local environment in L-In. In a flow cell, L-In shows a very small onset overpotential of ≈ 92 mV and delivers a current density of ≈ 360 mA cm⁻² with a formate Faradaic efficiency of 98% at a low potential of -0.62 V versus RHE. The formation rate of formate reaches up to $6364.4 \mu\text{mol h}^{-1} \text{mg}_{\text{In}}^{-1}$, which is nearly 39 folds higher than that of commercial In ($160.7 \mu\text{mol h}^{-1} \text{mg}_{\text{In}}^{-1}$), outperforming most of the previous results that have been reported under KHCO₃ environments. Density function theory calculations suggest that the defects facilitate the formation of *OCHO intermediate and stabilize the *HCOOH while inhibiting hydrogen adsorption. This study suggests that transient solid-state laser induction provides a facile and cost-effective approach to form ligand-free and defect-rich materials with tailored activities.


1. Introduction

Electrocatalytic carbon dioxide reduction (CO₂RR) to liquid fuels shows great potential to mitigate the rapid depletion of fossil resources.^[1] Among all the possible products of CO₂RR, formate is one of the most economically profitable products suggested by techno-economic analyses.^[2] However, the activation and reduction of CO₂ molecule to formate is typically hampered by the high energy barriers of CO₂ adsorption and subsequent bond cleavage, and the competing hydrogen evolution reaction (HER) that could reduce the Faradaic efficiency (FE).^[3] Therefore, the development of catalysts with high selectivity toward formate is necessary. P-block metal catalysts such as tin (Sn), bismuth (Bi), and indium (In) have been investigated for CO₂ reduction due to the fast electron transfer and favorable reaction barriers for formate production.^[4] Among

W. Guo, J. Su, Y. Song, L. Huang, L. Cheng, X. Cao, Y. Dou, Y. Ma, Z. Fan, R. Ye
Department of Chemistry
City University of Hong Kong
Hong Kong 999077, China
E-mail: ruquanye@cityu.edu.hk

Y. Zhang, Z. Zeng
Department of Materials Science and Engineering
City University of Hong Kong
Hong Kong 999077, China
E-mail: zhiyzeng@cityu.edu.hk

C. Ma, J. Dong
Beijing Synchrotron Radiation Facility
Institute of High Energy Physics
Chinese Academy of Sciences
Beijing 100049, China

 The ORCID identification number(s) for the author(s) of this article can be found under <https://doi.org/10.1002/smll.202201311>.

H. Zhu, Q. Liu
Department of Physics
City University of Hong Kong
Hong Kong 999077, China

T. Zheng, C. Xia
School of Materials and Energy
University of Electronic Science and Technology of China
Chengdu 610000, China

Z. Wang, B. Z. Tang
Shenzhen Institute of Aggregate Science and Technology
School of Science and Engineering
The Chinese University of Hong Kong
Shenzhen, Shenzhen City, Guangdong 518172, China

H. Li
Department of Physics
Technical University of Denmark
Lyngby 2800, Denmark

DOI: 10.1002/smll.202201311

these metals, indium is an ideal candidate for its high activity in catalyzing CO₂ to formic acid.^[4d,5] Different strategies, such as the formation of alloy,^[4b,5a,d,6] size controls,^[7] single atom,^[5d,8] and compositing with metal organic framework,^[9] have been employed to tune the CO₂RR performance of indium. These methods change the electronic structures and coordination numbers of the surface metal, which significantly improves the formate selectivity and current densities. However, achieving high formate selectivity, especially under an industrially relevant current density of >200 mA cm⁻² with low overpotential, remains challenging.^[4c,5b,d,7,8]

Defect engineering is an effective method to modulate the coordination environment and the electronic structure of metals.^[3a,10] Surface defects can regulate the electron density near the Fermi level and produce unsaturated coordination sites and dangling bonds, thus enhancing the adsorption capability toward the key intermediates.^[3a] Various strategies have been developed to produce defects, such as post-treatment, hard-templates,^[11] and direct pyrolysis.^[12] These methods often involve complex and laborious processes, such as etching, calcination, and ion exchange. In comparison, laser ablation is a facile and cost-effective method to produce materials with abundant defects.^[13] Using laser irradiation, various defects such as stacking fault,^[14] grain boundary,^[15] and vacancies,^[16] have been successfully induced and shown to improve the catalytic activities, most of which apply in water splitting. Research on the laser-induced formation of defective materials for CO₂RR remains underexplored. A recent report showed that laser irradiation of Sn and Cu alloy could improve the formate selectivity.^[4h] The activity was attributed to the change of electronic structure of Sn due to the adjacent Cu. However, the insufficient characterization at the atomic scale raises concerns that whether the activity comes from the alloying effect or surface defects. A thorough mechanistic understanding is pivotal for the rational design of electrocatalysts with enhanced CO₂RR performance.

Here we report a facile approach to prepare ligand-free and defect-rich indium nanoparticles (L-In) by transient laser induction of metal salts in the solid state. Conventional laser ablation methods repeatedly irradiate substrates underneath a liquid phase, which is time-consuming and could be affected by the liquid overlayer.^[13–14,17] In comparison, the solid-state pathway is fast and cost-effective. Spherical aberration-corrected high-resolution transmission electron microscope (HRTEM) images show the atomic structure of L-In, which contains abundant vacancies, self-interstitial defects, and stacking faults. X-ray absorption (XAS) at the L₃-edge of indium also discloses the undercoordinated feature of L-In. Theoretic calculation suggests that these defects can significantly reduce the energy barrier for forming the *OCHO intermediate, the critical step for CO₂-to-formate conversion. Consequently, L-In maintains a high formate FE of 98% even at an industrially relevant current density of 360 mA cm⁻². This performance is much higher than those prepared by the conventional wet-chemistry method (W-In) and commercial In (C-In). It is also superior to most of the reported P-block catalysts. Our work provides a cost-effective strategy to boost the CO₂RR performance of catalysts with high commercial potential.

2. Results and Discussion

Highly defective L-In is prepared handily by a laser ablation process (Figure 1a; see Method section for detail). The precursor is a mixture of indium chloride and carbon nanotube, the latter of which works as the conductive substrate and inhibits the agglomeration of indium into large particles. The transient laser heating induces the decomposition of indium salts into nanoparticles with a size of ≈13 nm (Figure S1a,b, Supporting Information). For comparison, we also prepared In nanoparticles via the conventional wet-chemistry method^[18] (W-In) with a size of ≈15 nm (Figures S3b and S4, Supporting Information), commercial In powder (C-In) and In oxide (C-In₂O₃).

Due to the kinetics effect and extreme conditions, transient laser heating will be beneficial to form non-crystalline features.^[19] Spherical aberration-corrected HRTEM is used to study the atomic structure of L-In (Figure 1b–g; additional images are shown in Figure S2, Supporting Information). Abundant defects are frequently observed, including a multitude of vacancies and self-interstitial defects. Figure 1c,f shows the self-interstitial defects and vacancies on the surface of L-In, designated by the blue and red circles, respectively. The intensity profiles along the highlighted area of Figure 1c,f are plotted in Figure 1g. In the red area, the significant decrease of intensity indicates the absence of In atom at the lattice point. These defects result in a highly strained surface and collectively change the layer spacing. As indicated in Figure 1g (bottom panel), the average distance along the direction shows that the abundant dislocated In atoms lead to a wide range of spacing from ≈1.7 to 1.39 Å. Stacking faults are also frequently observed on the surface, as highlighted in the yellow area of Figure 1d. For comparison, the HRTEM image of W-In (Figure S5, Supporting Information) reveals that the In atoms are highly ordered. The control sample of W-In highlights the advantage of transient laser heating in producing defect-rich nanomaterials.

X-ray diffraction (XRD; Figure 2a) and X-ray photoelectron spectroscopy (XPS; Figure S1c, Supporting Information) were used to characterize the structure and surface compositions of L-In. As shown in Figure 2a, the peak positions of In and CNT in the XRD patterns are well consistent with those of In-metal and CNT, respectively, which further confirms the successful formation of L-In nanostructures. The peak intensity of In is weaker than that of CNT due to the low loading of In. For the XPS analysis, the deconvolution of In 3d reveals the main contribution of In³⁺ with 3d_{5/2} and 3d_{3/2} at 446 and 453.3 eV, respectively. In⁰ can be observed from 3d_{5/2} and 3d_{3/2} located at 444.5 and 451.8 eV, respectively. This suggests the surface oxidation of indium. For W-In, the XRD (Figure S6a, Supporting Information) shows a similar signal of indium to that of L-In, and the XPS (Figure S6b, Supporting Information) also suggests the surface oxidation of indium with the contribution of In³⁺ 3d_{5/2} and 3d_{3/2}.

To further characterize the local environment and bonding characteristics of In atoms, X-ray absorption spectroscopy (XAS) at the In L₃-edge was carried out and compared to C-In₂O₃ and C-In (Figure 2). The structural characterizations of C-In₂O₃ and C-In are shown in Figures S7 and S8, Supporting Information. X-ray absorption near-edge structure (XANES) spectroscopy shows that the L-In at the In L₃-edge is very similar

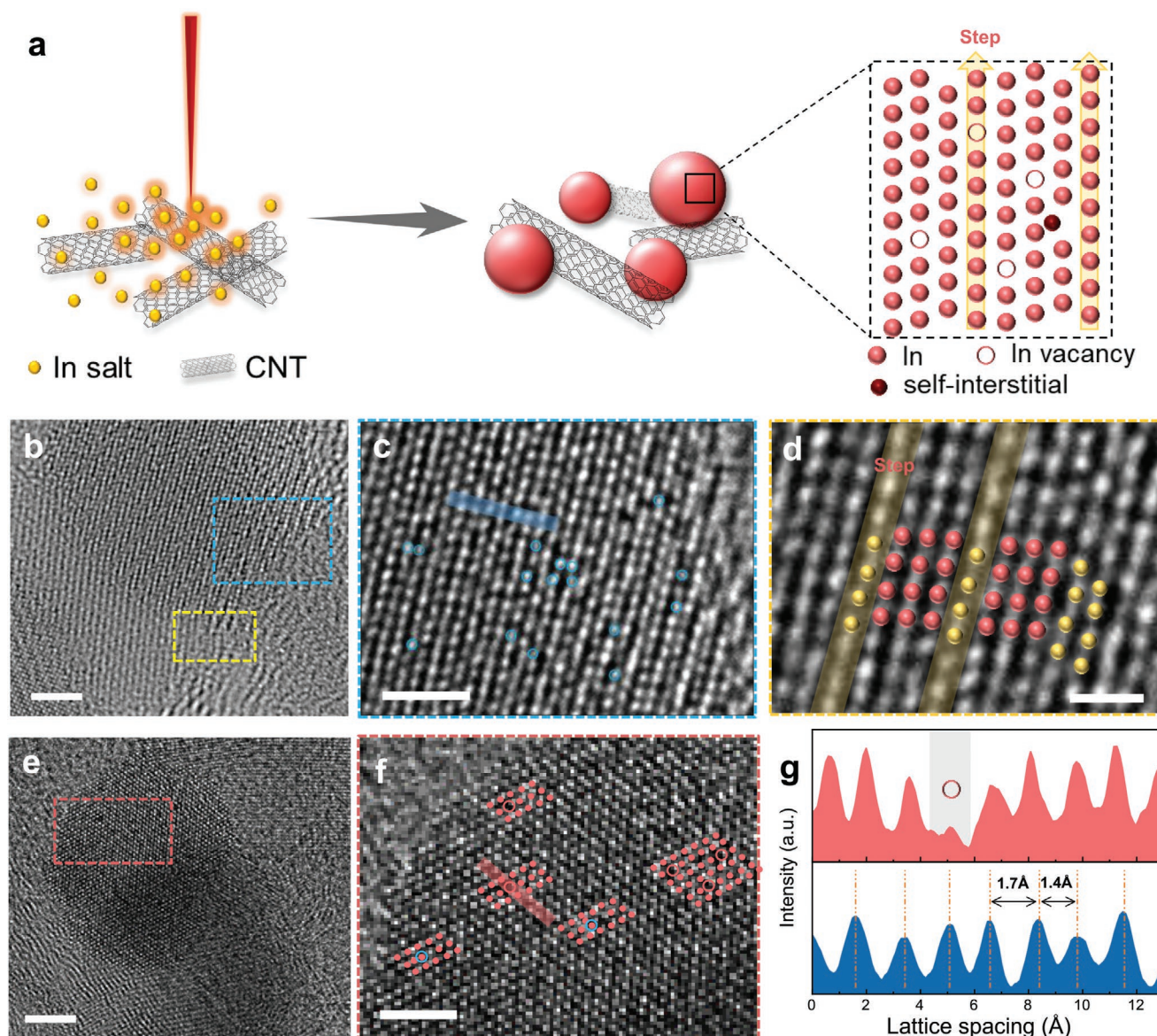


Figure 1. Preparation and characterization of L-In. a) Schematic for synthesizing L-In. b–f) Spherical aberration corrected HRTEM images of L-In showing the defects of vacancies, self-interstitial, and stacking faults. (c,d) are the enlarged area in (b) and (f) is the enlarged area in (e). g) The line intensity profile acquired along the red and blue areas in (c) and (f) respectively. Scale bar: 5 nm in (b,e); 1 nm in (c,f); 0.5 nm in (d).

to that of the C-In, suggesting a dominated In metal-like structure (Figure 2b). The peak positions of L-In from 3760 to 3850 eV are very close to those of C-In. However, the signal of L-In at 3748 eV is much weaker than C-In and C-In₂O₃, which indicates a poorer scattering due to the disordered and less-symmetry structure of L-In.^[20] Fourier-transformed extended X-ray absorption fine structure (EXAFS) spectrum (Figure 2c) reveals the bonding environment of indium atoms, featured with two main peaks at ≈ 2.2 Å and ≈ 3.2 Å corresponding to the In–O and In–In bond, respectively. Compared to C-In₂O₃, the In–O peak of L-In is significantly suppressed and the In–O bond length is also shorter, which is possibly due to the amorphous surface oxides. In reference to the C-In, the In–In peak intensity is also weaker, which indicates a smaller coordination number of indium atoms in L-In. The above microscopic

images and X-ray spectroscopies imply that the structure of L-In is closer to metallic indium with amorphous oxide at the surface, and the local environment of indium atoms is under-coordinated and highly defective.

Electrochemical performance was first characterized using a homemade three-electrode H-type cell in Ar or CO₂-saturated 0.5 M KHCO₃ electrolytes. During the initial scan, a cathodic wave is observed at -0.13 V versus a reversible hydrogen electrode (RHE; all the potentials are corrected to RHE hereafter), corresponding to the redox reaction of In³⁺/In⁰ (Figure S9, Supporting Information). This cathodic wave is attributed to the electrochemical reduction of surface oxide of L-In.^[7,21] As illustrated in Figure 3a, the CO₂RR polarization curve of L-In exhibits a low onset potential of -0.4 V versus RHE, and the current density rapidly reaches 15 mA cm⁻² at -0.8 V and

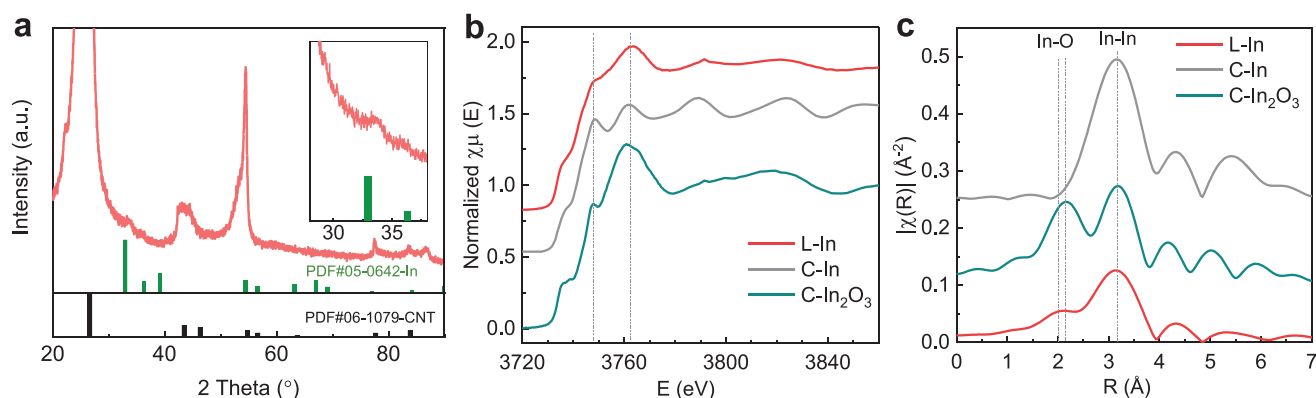


Figure 2. X-ray spectral analysis of L-In. a) XRD patterns of L-In. b) Normalized XANES and c) Fourier transformed EXAFS at the In L_3 -edge of L-In, C-In, and C-In $_2$ O $_3$.

38 mA cm $^{-2}$ at -1.2 V. In contrast, the polarization curve in Ar, which corresponds to the HER, is only 2.3 mA cm $^{-2}$ at -0.8 V. Such significant differences immediately indicates that L-In strongly favors CO $_2$ RR over HER. For comparison, C-In and W-In were tested under the same conditions as shown in Figure 3a. Compared with C-In (18 mA cm $^{-2}$ at -1.2 V) and W-In (22 mA cm $^{-2}$ at -1.2 V), the superior performance of L-In implies that the unique structure and coordination environments of L-In are more efficient for CO $_2$ reduction. Chronoamperometry between -0.4 V and -1.2 V was performed. The FE $_{CO}$ and FE $_{H_2}$ for different samples were shown in Figures S10 and S11, Supporting Information, and the FE $_{formate}$ were sum-

marized in Figure 3b. Bare carbon plate and bare CNT on carbon plate produce exclusively H $_2$ (Figures S12 and S13, Supporting Information). L-In exhibits the highest FE $_{formate}$ at all the applied potentials in comparison to other control materials. Specifically, L-In's initial formate FE maintains above 93% in a wide potential window ranging from -0.73 V to -1.13 V, which is significantly greater than C-In ($\approx 43\%$ at -0.93 V) and W-In ($\approx 63\%$ at -1.03 V). The formate partial current densities and mass production rate are further compared (Figure 3c,d). L-In delivers 32 mA cm $^{-2}$ at -1.13 V, which is equivalent to a high value of 6364.4 μ mol h $^{-1}$ mg $_{In}^{-1}$ (the catalyst loading is confirmed by ICP-AES result, see Table S1, Supporting Information). This

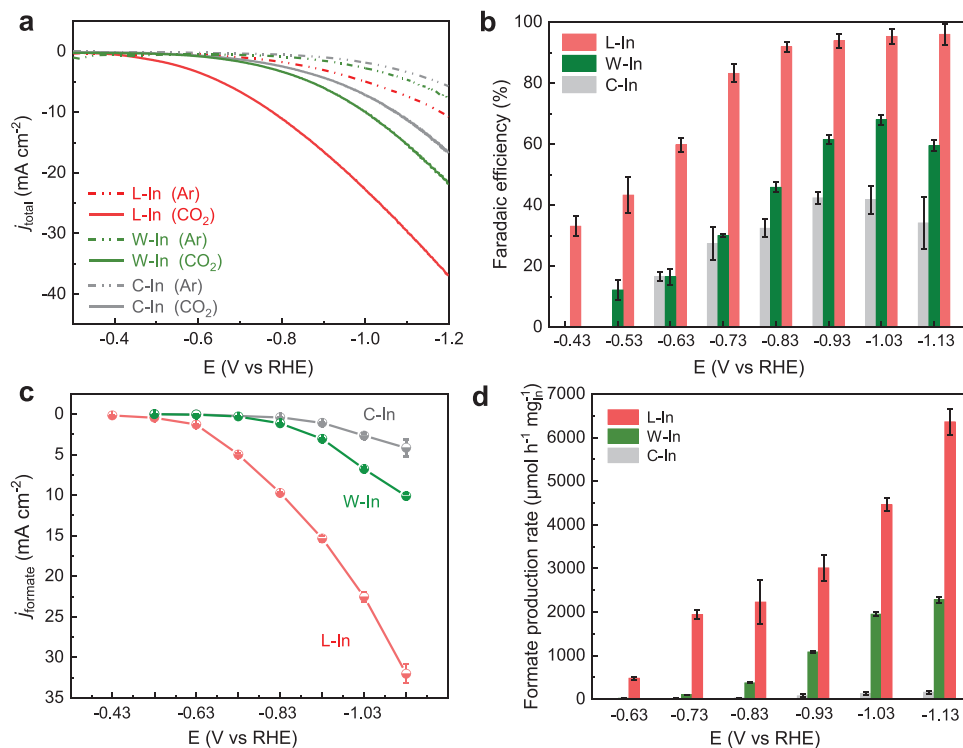


Figure 3. Electrochemical carbon dioxide reduction measurements in the H-type cell. a) Polarization curves of L-In, W-In, and C-In at a scan rate of 10 mV s $^{-1}$ in Ar- (dotted line) and CO $_2$ -saturated (solid line) 0.5 M KHCO $_3$ electrolyte. b) Faradaic efficiencies of formate, c) formate partial current density, and d) formate production rate of L-In, W-In, and C-In at different potentials.

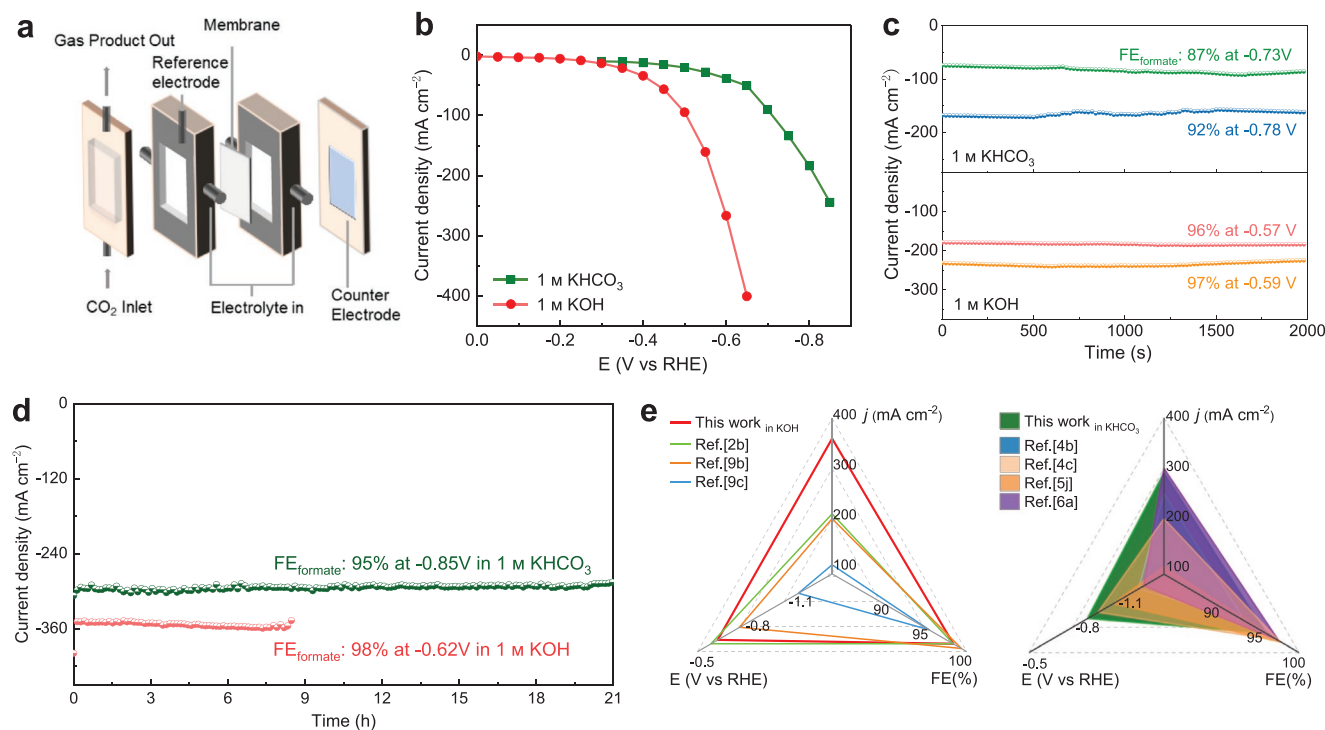


Figure 4. Electrochemical carbon dioxide reduction measurements in the flow cell. a) Diagram of gas diffusion electrolysis cell. b) Polarization curve of L-In in 1 M KHCO₃ or 1 M KOH at a scan rate of 50 mV s⁻¹. c) Chronoamperometric response and FE under different potentials. d) Long-term stability test in 1 M KHCO₃ or 1 M KOH. e) Comparison of the potential, FE, and current density of L-In to literature data in flow cell. The solid lines refer to using KOH as the electrolyte and the filled areas refer to KHCO₃ (see Table S2 for details, Supporting Information).

performance is nearly 3 and 39 folds higher than those of W-In (2284.6 $\mu\text{mol h}^{-1} \text{mg}_{\text{In}}^{-1}$) and C-In (160.7 $\mu\text{mol h}^{-1} \text{mg}_{\text{In}}^{-1}$). The outstanding current density and FE of L-In at the whole examined potentials highlight the pivotal role of defects in improving the formate selectivity for CO₂RR.

The mass transport issues can limit the CO₂RR performance using the H-cell, which can be mitigated by using the gas diffusion layer in a flow cell (Figure 4a). The flow cell enables CO₂ to directly and quickly diffuse to the solid-liquid-gas three-phase boundary, which improves catalytic performance.^[21,22] L-In exhibits excellent current densities and FEs in the flow cell in 1 M KHCO₃ or KOH electrolyte. The polarization curve of L-In starts from -0.4 V in 1 M KHCO₃, similar to that in H-cell. However, its current density dramatically increases from $\approx 10 \text{ mA cm}^{-2}$ to $\approx 250 \text{ mA cm}^{-2}$ at -0.83 V, corresponding to an increase of >20 folds (Figure 4b). Faradaic efficiencies toward CO and H₂ based on L-In in 1 M KHCO₃ or 1 M KOH in the flow cell are shown in Figure S14, Supporting Information. The FE_{formate} is 87% at -0.73 V and 92% at -0.78 V, respectively, indicating that the increase in current density mainly comes from formate production (Figure 4c top). When tested in 1 M KOH, the onset potential is significantly reduced to -0.2 V, and the current density reaches 360 mA cm⁻² at -0.62 V. This corresponds to an overpotential of 92 mV and highlights the high activity of L-In in achieving high current density at a very low potential (Figure 4b). In addition, the selectivity of formate is improved to 96% at -0.57 V and 97% at -0.59 V, respectively (Figure 4c bottom), which is mainly because of the inhibition of HER in alkaline electrolyte.^[22c,23]

In addition to the unusual activity and selectivity, L-In also exhibits excellent durability and works steadily under high current density with FE_{formate} > 95% for at least 21 h in 1 M KHCO₃ at a potential of -0.85 V, and an average formate selectivity of 98% can be maintained at the potential of -0.62 V for 8 h in 1 M KOH with a high current density of $\approx 360 \text{ mA cm}^{-2}$. After 8 h, some white crystals formed on the hydrophobic surface of GDL, which affected the stability as previously reported.^[2b] The white crystal may be the bicarbonate or carbonate. It is mainly because OH⁻ and CO₂ easily form HCO₃⁻ or CO₃²⁻, precipitating on the back of the catalyst with time, which hinders the adsorption of CO₂, and then affect the catalytic efficiency and catalyst's stability (Note 1S, Supporting Information).^[24] The nanoparticles of L-In after 21 h stability test are slightly larger (Figure S15, Supporting Information) and XRD pattern shows a stronger In metal (Figure S16, Supporting Information), which could be because of the reduction of amorphous oxide during CO₂RR. It is worth mentioning that the defects still maintained after the stability even though the size of L-In increased (Figure S17, Supporting Information). We also compare the potential, FE, and current density with other reported catalysts shown in Figure 4e. For example, the NDT-Bi exhibited 98% formate selectivity at -0.58 V, and the current density was 210 mA cm⁻².^[2b] The ZnIn₂S₄ achieved 97% formate FE and a current density of 300 mA cm⁻² at -1.18 V.^[6a] (see Table S2, Supporting Information for details). The L-In is among the best-performing catalysts, especially in light of the high current densities (360 mA cm⁻²) at a very low potential (-0.62 V) with $\approx 95\%$ FE_{formate}.

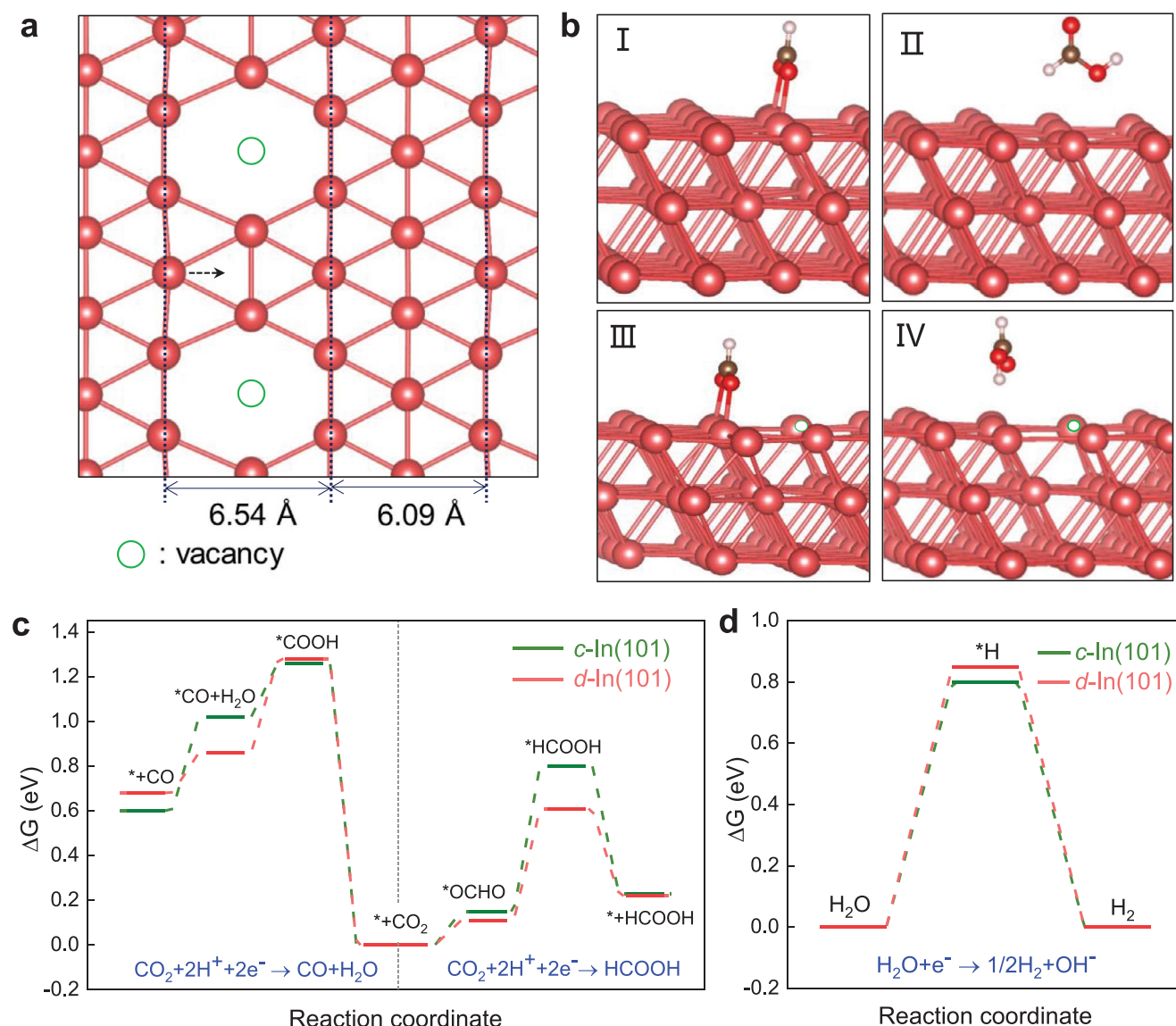


Figure 5. DFT calculation on crystalline and defective In (101) surface. a) Optimized structure of *d*-In (101). b) Optimized geometric structures of *OCHO (I), HCOOH (II) on ideal *c*-In (101) surface and *OCHO (III), HCOOH (IV) on defective *d*-In (101) surface. The coral, brown, red, white balls, and green circle represent In, C, O, H, and In vacancy, respectively. c) Calculated free energy diagrams for CO₂RR and d) HER on ideal and defective In (101) surfaces.

DFT calculations were performed to provide theoretical insights into the outstanding CO₂RR performance. The module used the In (101) facet that was previously determined to have the lowest surface energy.^[5b] We calculated the free energy diagram using the crystalline and defective facets, designated as *c*-In (101) and *d*-In (101), respectively. The structure of *d*-In (101) is shown in **Figure 5a**. For a slab of 36 In atoms, one surface In atom is removed to represent the defective *d*-In (101). Optimization of *d*-In (101) results in the dislocations of atoms and the change of lattice spacing, which are consistent with the microscopic images (Figure 1b–g). Figure 5b and Figure S18, Supporting Information, show the structure of intermediates for CO₂RR and HER, and the energies of reaction coordinations are summarized in Figure 5c,d. On the *c*-In (101) surface, the rate-determining step for producing formic acid is the

formation of *HCOOH intermediate with an energy barrier of 0.8 eV, while the rate-determining step for producing CO is the formation of *COOH intermediate with a barrier of 1.26 eV (Figure 5c). In addition, the competitive hydrogen evolution reaction (Figure 5d) also has a higher energy barrier of 0.78 eV than the formation of HCOOH. Therefore, *c*-In (101) surface is more conducive to the production of HCOOH than CO and H₂, which is also in line with the experimental data.

The same reaction steps are also calculated on the *d*-In (101) surface. Compared to the *c*-In (101), the reaction energy barrier for forming *HCOOH on the defective In (101) surface is lowered to 0.61 eV, implying the more favorable HCOOH production. Meanwhile, the energy barrier for forming *COOH on the *d*-In (101) surface remains as high as 1.28 eV, suggesting that the defects do not improve the CO production. Also, the

energy for generating *H is significantly uphill to 0.85 eV, indicating HER is further suppressed on the defective surface. Noting that the most energetically favorable configuration for *COOH is the binding of one C to one In atom, while *OCHO is the binding of two O atoms via two In atoms, which may be the reason for *OCHO has a stronger interaction with the metals. In short, our calculation agrees with the literature that the reaction pathway of CO_2 -to-formate conversion is through the *OCHO intermediates.^[2a] The defective d -In (101) surface is undercoordinated; it has a small *OCHO formation energy barrier and stabilizes the *HCOOH intermediate, thereby facilitating the production of $HCOOH$ and exhibiting higher performance of CO_2 -to- $HCOOH$ conversion.

3. Conclusion

In conclusion, we have developed a facile, fast, yet effective solid-state laser activation method to synthesize the L-In with rich defects. The L-In enables the high-performance CO_2 reduction toward formate, showing a formate production rate of up to $6364.4 \mu\text{mol h}^{-1} \text{mg}_{\text{In}}^{-1}$ in 0.5 M KHCO_3 with a H-cell and reaching a current density of 300 mA cm^{-2} at -0.85 V in 1 M KHCO_3 and 360 mA cm^{-2} at -0.62 V in 1 M KOH in a flow cell. The spherical aberration-corrected HRTEM image and XAS study show that L-In contains abundant defects, which change the surface electronic structures and the coordination environments of indium. Further electrochemical characterizations combined with DFT calculations reveal that the defective L-In suppresses the HER and facilitates the formation of *OCHO to produce formate. Our study here provides a facile yet powerful way to boost the catalytic performance of the metal and discloses the significant influence of defects on catalytic activity. It also has implications for designing other electrocatalysts using transient laser activation.

4. Experimental Section

Materials: All chemicals were directly used without further purifications. Indium chloride (InCl_3), Indium acetylacetonate ($\text{In}(\text{acac})_3$), oleylamine (80–90%), Indium oxide (In_2O_3) and Indium powder were purchased from Macklin. Potassium bicarbonate (KHCO_3) and potassium hydroxide (KOH) were purchased from Alfa Aesar. Cyclohexane and ethanol were from Sinopharm Chemical Reagent Co., China.

Synthesis of Laser-Indium (L-In) NPs: A $10.6 \mu\text{m}$ CO_2 laser marking machine (Minsheng Laser #MSDB-FM60 CO_2 Laser Marker, 60 W) was used to convert the indium salt to L-In NPs. The laser parameters were set as follows: laser power 1.8 W , speed 1000 mm s^{-1} , and line spacing 0.03 mm . Specially, first, 0.5 M InCl_3 was prepared with ethanol, and then add carbon nanotubes to prepare a 5 mg mL^{-1} carbon ink. After sonicating with an ultrasonic machine for 20 minutes and mixing uniformly, $80 \mu\text{L}$ of the solutions were dropped onto the two sides of the diameter of 1.13 cm carbon paper respectively. Then an infrared lamp was used to dry the carbon paper. After the surface ethanol evaporates, the carbon paper with InCl_3/CNT was irradiated with a $10.6 \mu\text{m}$ CO_2 laser marking machine to fabricate L-In. Then L-In was used for the next characterization.

Synthesis of In Nanoparticles (W-In): First added $50 \text{ mg In}(\text{acac})_3$, 5 mL oleylamine and 50 mg NaBH_4 into a 20 mL round bottom flask and then heated the mixture at 120° for 2 h .^[18] After cooling, it was divided into two tubes and centrifuged 3 times at 12800 rpm for 15 mins with

ethanol to remove impurities. Then carbon nanotubes were added to prepare a 5 mg mL^{-1} carbon ink for the next characterization.

Structure Characterizations: Crystal structures of the materials were determined by X-ray diffraction (XRD) patterns, which were collected by a Bruker D2 with $\text{Cu K}\alpha$ radiation. The X-ray photoelectron spectroscopy (XPS) data were collected on a Thermo ESCALAB 250Xi spectrometer equipped with a monochromatic AlK radiation source (1486.6 eV , pass energy 20.0 eV). The data were calibrated with C $1s$ 284.8 eV . The scanning electron microscopy (SEM) images were collected by a Thermo Scientific Quattro S operated at 20 kV . The energy dispersive X-ray spectroscopy (EDS) elemental mappings were taken on a JEOL 2100F (Japan) operated at 200 kV . The high-resolution TEM (HRTEM) images were acquired by spherical-aberration-corrected FEI Themis Z microscope operated at 80 kV . The loading amount of In was confirmed with an inductively coupled plasma optical emission spectrometry (ICP-OES, PerkinElmer, Optima 8000). The XAFS spectra at the In L_3 -edge were acquired at station 4B7A of the Beijing Synchrotron Radiation Facility operated at 2.2 GeV with a maximum current of 250 mA and recorded in total electron yield mode by collecting the sample drain current.

Electrochemical Measurements: The self-made three-electrode electrochemical cell was used for electrochemical performance. The anode and cathode compartments was separated by Nafion-117 proton exchange membrane, with the diameter of 1.13 cm carbon plate loading with L-In as the working electrode. The counter electrode was platinum plate and reference electrode was nonleakage Ag/AgCl electrode. The reference electrode nonleakage Ag/AgCl electrode was calibrated in a high-purity hydrogen-saturated electrolyte, Pt wire was used as the working electrode, and the scan rate was 1 mV s^{-1} . The average of the two potentials of each CV curve where the current was zero was regarded as the thermodynamic potential. All measured potentials were converted to reversible hydrogen electrode (RHE) scale by calibration using the following equation: $E (\text{versus RHE}) = E (\text{versus Ag}/\text{AgCl}) + 0.059 \text{ pH} + 0.261 \text{ V}$. The electrolyte was used 1.75 mL 0.5 M KHCO_3 solution, purged with CO_2 for 10 min before electrochemical polarization. CHI650E potentiostat was used to record the electrochemical response. The resistance between the reference electrode and the working electrode was measured by potentiometric electrochemical impedance spectroscopy (PEIS) and manually compensated for 95%. During the electrocatalytic CO_2 RR experiment, CO_2 was steadily bubbled into the electrochemical cell at a rate of 10 sccm . Gas products were measured by an online gas chromatograph (Ruimin GC 2060), which contains a Haysep-D column, a TCD detector for H_2 quantification and a FID detector for CO quantification.

$$FE_{\text{gas}} = \frac{Q_{\text{HCOO}^-}}{Q_{\text{total}}} \times 100\% = \frac{n_{\text{gas}} \times N \times F}{j \times t} \times 100\% = \frac{P}{RT} \times \frac{N \times F}{j} \times \nu \times 100\% \quad (1)$$

n_{gas} is the amount of gas (mol), $N = 2$ is the number of electron transfer to form a molecule of CO or H_2 , $F = 95200 \text{ C mol}^{-1}$ is Faraday constant, P is the atmosphere pressure (Pa), $T = 298 \text{ K}$ is the temperature (K) and R is the molar gas constant $= 8.31 \text{ J mol}^{-1} \text{ K}^{-1}$, ν is the gas flow rate, j is the total current.

The liquid products were analyzed afterward by quantitative NMR (Bruker AVANCE III 300). The peak area of the product with the internal standard to make a standard curve, using DMSO as the internal standard and deuterated water to suppress the water peak was compared.^[25] After electrolysis, 0.45 mL electrolyte was mixed with $50 \mu\text{L}$ DMSO (10 mM , internal standard) in D_2O (99.9%, Sigma-Aldrich) for the NMR analysis. All quantitative spectra used the same spectrum acquisition parameters. The formula was added for calculating formate faradaic efficiency is as follows:

$$FE_{\text{HCOO}^-} = \frac{Q_{\text{HCOO}^-}}{Q_{\text{total}}} \times 100\% = \frac{n_{\text{HCOO}^-} \times N \times F}{j \times t} \times 100\% \quad (2)$$

$N = 2$ is the number of electron transfer to form a molecule of $HCOO^-$; $F = 95200 \text{ C mol}^{-1}$ is the Faraday constant, j is the total current.

Flow Cell Measurements: The flow cell contained a gas-diffusion layer (GDL), an anion exchange membrane (Fumasep FAA-3-PK-130), the platinum plat (15 × 35 × 0.2 mm) as the counter electrode, and a leak-free Ag/AgCl electrode as a reference electrode. The working electrodes were prepared by dropping 320 µl of catalyst ink (5 mg mL⁻¹) onto the microporous side of the GDL to reach a total mass loading of L-In loaded-GDL (1 mg cm⁻², 0.5 cm × 2 cm). 1 M KHCO₃ or 1 M KOH the electrolytes were separately circulated in both the working and counter compartments using peristaltic pumps (Longer, BT100-2J) at flow rates of 5 mL min⁻¹ and 20 mL min⁻¹, respectively. The CO₂ flow was kept constant at 30 sccm using a mass flow controller. A CHI650E potentiostat was employed to record the electrochemical responses. The electrolyte resistance between the reference electrode and working electrode was determined to be ≈3.5–5 Ω using potential electrochemical impedance spectroscopy (PEIS) analysis and automatically compensated. The gas products were analyzed by an online gas chromatograph. The liquid products were analyzed afterward by quantitative NMR (Bruker AVANCE III 300).

Computation: First-principles calculations based on the density functional theory (DFT) were simulated with the Vienna ab-initio simulation package (VASP),^[26] using projected augmented wave (PAW) potentials.^[27] The revised Perdew, Burke, and Ernzerhof exchange-correlation functional within a generalized gradient approximation (GGA-RPBE) was used to describe the exchange-correlation energy.^[28] An energy cutoff of 500 eV was used for the expansion of wavefunctions over the plane-wave basis set.

All structures were fully relaxed until the force on each atom was less than 0.01 eV Å⁻¹ and the energy is 10⁻⁵ eV per atom. The vacuum space was set to 15 Å in the z-direction to avoid the periodic influence, and the Brillouin zone integration was performed on 5 × 10 × 1 and 3 × 2 × 1 Monkhorst–Pack k-point meshes for the unit cell and supercell structure, respectively. a (101) surface of Indium (In(101) surface) was chosen as the substrate to study its electrocatalytic performance. In(101) surface was built using three-layer model in a 2 × 3 supercell, with the bottom layer fixed during optimization while the remaining atoms relaxed.

The reaction pathways for the production HCOOH and CO were simulated as follows (where asterisk * represents the active catalytic site on the surface)

CO generation:



HCOOH generation:



The Gibbs free energy change (ΔG) was calculated by employing Nørskov's computational hydrogen electrode model.^[29]

The equation as follows:

$$\Delta G = \Delta E + \Delta E_{\text{ZPE}} - T\Delta S + \Delta G_{\text{pH}} \quad (9)$$

where ΔE is the reaction energy gained from the DFT calculations, ΔE_{ZPE} and ΔS are the difference of zero-point energy and entropy, respectively. T is the temperature (298.15 K). ΔG_{pH} = 2.303k_BTpH, where k_B was the Boltzmann constant, and pH was assumed to be zero for acidic conditions.

Statistical Analysis: The Faradaic efficiencies were calculated from the average of three measurements.

Supporting Information

Supporting Information is available from the Wiley Online Library or from the author.

Acknowledgements

This work was supported by the Guangdong Basic and Applied Basic Research Fund (2022A1515011333), the Science, Technology, and Innovation Commission of Shenzhen under Shenzhen Virtual University Park Special Fund (No. 2021Szvup129), and the Hong Kong Research Grant Council under Early Career Scheme (No. 21300620). C.X. acknowledges the National Natural Science Foundation of China (22102018 and 52171201), the Central Government Funds of Guiding Local Scientific and Technological Development for Sichuan Province (no. 2021ZYD0043), and the University of Electronic Science and Technology of China for startup funding (A1098531023601264). B.Z.T. thanks the support from Shenzhen Key Laboratory of Functional Aggregate Materials (ZDSYS20211021111400001). R.Y. conceived the idea. W.G. conducted sample preparation and characterization with assistance from J.S., Y.S., L.H., L.C., X.C., Y.D., Y.M., G.L. H.Z., T.Z., Z.W., Z.F., Q.L., and B.T. C.M., and J.D. obtained the XAS data, Y. Z., H.L., and Z.Z. performed the theoretical calculations. W.G. and R.Y. wrote the manuscript with comments from all the authors.

Conflict of Interest

The authors declare no conflict of interest.

Data Availability Statement

The data that support the findings of this study are available from the corresponding author upon reasonable request.

Keywords

abundant defects, carbon dioxide reduction reaction, industrial-relevance formate production rate, laser activation, low overpotential

Received: March 1, 2022

Revised: April 28, 2022

Published online: May 13, 2022

- [1] a) C. E. Finke, H. F. Leandri, E. T. Karumb, D. Zheng, M. R. Hoffmann, N. A. Fromer, *Energy Environ. Sci.* **2021**, 14, 1517; b) D. Gao, R. M. Arán-Ais, H. S. Jeon, B. Roldan Cuenya, *Nat. Catal.* **2019**, 2, 198; c) F. P. Pan, Y. Yang, *Energy Environ. Sci.* **2020**, 13, 2275; d) S. Chu, A. Majumdar, *Nature* **2012**, 488, 294; e) C. Liu, Colón, B. C., Ziesack, M., Silver, P. A., Nocera, D. G., *Science* **2016**, 352, 1210.
- [2] a) Z. N. Yang, F. E. Oropeza, K. H. L. Zhang, *APL Mater.* **2020**, 8, 060901; b) Q. Gong, P. Ding, M. Xu, X. Zhu, M. Wang, J. Deng, Q. Ma, N. Han, Y. Zhu, J. Lu, Z. Feng, Y. Li, W. Zhou, Y. Li, *Nat. Commun.* **2019**, 10, 2807; c) O. S. Bushuyev, P. De Luna, C. T. Dinh, L. Tao, G. Saur, J. van de Lagemaat, S. O. Kelley, E. H. Sargent, *Joule* **2018**, 2, 825.
- [3] a) Q. C. Wang, Y. P. Lei, D. S. Wang, Y. D. Li, *Energy Environ. Sci.* **2019**, 12, 1730; b) C. Xia, P. Zhu, Q. Jiang, Y. Pan, W. T. Liang, E. Stavitski, H. N. Alshareef, H. T. Wang, *Nat. Energy* **2019**, 4, 776.

- [4] a) C. W. Lee, K. D. Yang, D. H. Nam, J. H. Jang, N. H. Cho, S. W. Im, K. T. Nam, *Adv. Mater.* **2018**, *30*, 1704717; b) Y. Xing, X. Kong, X. Guo, Y. Liu, Q. Li, Y. Zhang, Y. Sheng, X. Yang, Z. Geng, J. Zeng, *Adv. Sci.* **2020**, *7*, 1902989; c) L. Fan, C. Xia, P. Zhu, Y. Lu, H. Wang, *Nat. Commun.* **2020**, *11*, 3633; d) N. Han, P. Ding, L. He, Y. Li, Y. Li, *Adv. Energy Mater.* **2019**, *10*, 1902338; e) W. Zhang, S. Yang, M. Jiang, Y. Hu, C. Hu, X. Zhang, Z. Jin, *Nano Lett.* **2021**, *21*, 2650; f) X. Zheng, P. De Luna, F. P. García de Arquer, B. Zhang, N. Becknell, M. B. Ross, Y. Li, M. N. Banis, Y. Li, M. Liu, O. Voznyy, C. T. Dinh, T. Zhuang, P. Stadler, Y. Cui, X. Du, P. Yang, E. H. Sargent, *Joule* **2017**, *1*, 794; g) N. Han, Y. Wang, H. Yang, J. Deng, J. Wu, Y. Li, Y. Li, *Nat. Commun.* **2018**, *9*, 1320; h) M. Ren, H. Zheng, J. Lei, J. Zhang, X. Wang, B. I. Yakobson, Y. Yao, J. M. Tour, *ACS Appl. Mater. Interfaces* **2020**, *12*, 41223; i) T. Ma, Z. Wu, H. Wu, W. Cai, Z. Wen, L. Wang, W. Jin, B. Jia, *Angew. Chem., Int. Ed.* **2021**, *60*, 12554; j) J. Yan, Y. X. Duan, Z. Yu, Q. Jiang, Y. T. Zhou, D. X. Liu, Z. Wen, *Angew. Chem., Int. Ed.* **2021**, *60*, 8798.
- [5] a) Z. B. Hoffman, T. S. Gray, K. B. Moraveck, T. B. Gunnoe, G. Zangari, *ACS Catal.* **2017**, *7*, 5381; b) W. Ma, S. Xie, X. G. Zhang, F. Sun, J. Kang, Z. Jiang, Q. Zhang, D. Y. Wu, Y. Wang, *Nat. Commun.* **2019**, *10*, 892; c) L. Wang, L. Wang, Y. Du, X. Xu, S. X. Dou, *Mater. Today Phys.* **2021**, *16*, 100294; d) W. Guo, X. Tan, J. Bi, L. Xu, D. Yang, C. Chen, Q. Zhu, J. Ma, A. Tayal, J. Ma, Y. Huang, X. Sun, S. Liu, B. Han, *J. Am. Chem. Soc.* **2021**, *143*, 6877; e) H. F. Liu, J. Xia, N. Zhang, H. Cheng, W. T. Bi, X. L. Zu, W. S. Chu, H. A. Wu, C. Z. Wu, Y. Xie, *Nat. Catal.* **2021**, *4*, 202; f) A. Zhang, Y. Liang, H. Li, X. Zhao, Y. Chen, B. Zhang, W. Zhu, J. Zeng, *Nano Lett.* **2019**, *19*, 6547; g) S. He, F. Ni, Y. Ji, L. Wang, Y. Wen, H. Bai, G. Liu, Y. Zhang, Y. Li, B. Zhang, H. Peng, *Angew. Chem., Int. Ed.* **2018**, *57*, 16114; h) W. X. Ma, J. Bu, Z. P. Liu, C. Yan, Y. Yao, N. H. Chang, H. P. Zhang, T. Wang, J. Zhang, *Adv. Funct. Mater.* **2020**, *31*, 2006704.
- [6] a) L. P. Chi, Z. Z. Niu, X. L. Zhang, P. P. Yang, J. Liao, F. Y. Gao, Z. Z. Wu, K. B. Tang, M. R. Gao, *Nat. Commun.* **2021**, *12*, 5835; b) W. J. Dong, C. J. Yoo, J. L. Lee, *ACS Appl. Mater. Interfaces* **2017**, *9*, 43575.
- [7] Y. Huang, X. Mao, G. Yuan, D. Zhang, B. Pan, J. Deng, Y. Shi, N. Han, C. Li, L. Zhang, L. Wang, L. He, Y. Li, Y. Li, *Angew. Chem., Int. Ed.* **2021**, *60*, 15844.
- [8] a) P. Lu, X. Tan, H. Zhao, Q. Xiang, K. Liu, X. Zhao, X. Yin, X. Li, X. Hai, S. Xi, A. T. S. Wee, S. J. Pennycook, X. Yu, M. Yuan, J. Wu, G. Zhang, S. C. Smith, Z. Yin, *ACS Nano* **2021**, *15*, 5671; b) T. T. Zheng, C. X. Liu, C. X. Guo, M. L. Zhang, X. Li, Q. Jiang, W. Q. Xue, H. L. Li, A. W. Li, C.-W. Pao, J. P. Xiao, C. Xia, J. Zeng, *Nat. Nanotechnol.* **2021**, *16*, 1386.
- [9] a) Y. Zhou, S. Liu, Y. Gu, G. H. Wen, J. Ma, J. L. Zuo, M. Ding, *J. Am. Chem. Soc.* **2021**, *143*, 14071; b) C. Cao, D. D. Ma, J. F. Gu, X. Xie, G. Zeng, X. Li, S. G. Han, Q. L. Zhu, X. T. Wu, Q. Xu, *Angew. Chem., Int. Ed.* **2020**, *59*, 15014; c) Z. Wang, Y. Zhou, C. Xia, W. Guo, B. You, B. Y. Xia, *Angew. Chem., Int. Ed.* **2021**, *60*, 19107.
- [10] a) X. Lou, S. Li, X. Chen, Q. Zhang, H. Deng, J. Zhang, D. Li, X. Zhang, Y. Zhang, H. Zeng, G. Tang, *ACS Nano* **2021**, *15*, 8204; b) M. D. Armstrong, K. W. Lan, Y. Guo, N. H. Perry, *ACS Nano* **2021**, *15*, 9211.
- [11] Y. Jiang, L. Yang, T. Sun, J. Zhao, Z. Lyu, O. Zhuo, X. Wang, Q. Wu, J. Ma, Z. Hu, *ACS Catal.* **2015**, *5*, 6707.
- [12] H. B. Yang, J. W. Miao, S.-F. Hung, J. Z. Chen, H. B. Tao, *Sci. Adv.* **2016**, *2*, 1501122.
- [13] V. Amendola, D. Amans, Y. Ishikawa, N. Koshizaki, S. Scire, G. Compagnini, S. Reichenberger, S. Barcikowski, *Chem. - Eur. J.* **2020**, *26*, 9206.
- [14] Z. Li, J.-Y. Fu, Y. Feng, C.-K. Dong, H. Liu, X.-W. Du, *Nat. Catal.* **2019**, *2*, 1107.
- [15] a) E. Boutin, L. Merakeb, B. Ma, B. Boudy, M. Wang, J. Bonin, E. Anxolabehere-Mallart, M. Robert, *Chem. Soc. Rev.* **2020**, *49*, 5772; b) C. Tang, P. Gong, T. Xiao, Z. Sun, *Nat. Commun.* **2021**, *12*, 2139.
- [16] Q. Kang-Wen, C. Xi, Y. Zhang, R. Zhang, Z. Li, G. R. Sheng, H. Liu, C. K. Dong, Y. J. Chen, X. W. Du, *Chem. Commun.* **2019**, *55*, 8579.
- [17] a) Z. Li, Y. Feng, Y. L. Liang, C. Q. Cheng, C. K. Dong, H. Liu, X. W. Du, *Adv. Mater.* **2020**, *32*, 1908521; b) D. Zhang, B. Gokce, S. Barcikowski, *Chem. Rev.* **2017**, *117*, 3990.
- [18] S. Dreyfuss, C. Pradel, L. Vendier, S. Mallet-Ladeira, N. Mezaillies, *Chem. Commun.* **2016**, *52*, 14250.
- [19] a) L. Cheng, W. H. Guo, X. H. Cao, Y. B. Dou, L. B. Huang, Y. Song, J. J. Su, Z. Y. Zeng, R. Q. Ye, *Mater. Chem. Front.* **2021**, *5*, 4874; b) X. Han, R. Q. Ye, Y. Chyan, T. Wang, C. H. Zhang, L. L. Shi, T. Zhang, Y. Zhao, J. M. Tour, *ACS Appl. Nano Mater.* **2018**, *1*, 5053; c) Y. Chyan, R. Q. Ye, Y. L. Li, S. P. Singh, C. J. Arnusch, J. M. Tour, *ACS Nano* **2018**, *12*, 2176.
- [20] Y. J. Sa, S. O. Park, G. Y. Jung, T. J. Shin, H. Y. Jeong, S. K. Kwak, S. H. Joo, *ACS Catal.* **2018**, *9*, 83.
- [21] B. B. Pan, G. T. Yuan, X. Zhao, N. Han, Y. Huang, K. Feng, C. Cheng, J. Zhong, L. Zhang, Y. H. Wang, Y. G. Li, *Small Sci.* **2021**, *1*, 2100029.
- [22] a) B. Martindale, *Nat. Catal.* **2020**, *3*, 966; b) K. J. P. Schouten, *Nat. Energy* **2021**, *6*, 335; c) J. J. Su, J.-J. Zhang, J. C. Chen, Y. Song, L. B. Huang, M. H. Zhu, B. I. Yakobson, B. Z. Tang, R. Q. Ye, *Energy Environ. Sci.* **2021**, *14*, 483.
- [23] M. H. Zhu, J. C. Chen, L. B. Huang, R. Q. Ye, J. Xu, Y. F. Han, *Angew. Chem., Int. Ed.* **2019**, *58*, 6595.
- [24] a) Y. Hori, H. Ito, K. Okano, K. Nagasu, S. Sato, *Electrochim. Acta* **2003**, *48*, 2651; b) L. M. Aeshala, R. Uppaluri, A. Verma, *Phys. Chem. Chem. Phys.* **2014**, *16*, 17588.
- [25] K. P. Kuhl, E. R. Cave, D. N. Abram, T. F. Jaramillo, *Energy Environ. Sci.* **2012**, *5*, 7050.
- [26] G. Kresse, J. Hafner, *Phys. Rev. B* **1994**, *49*, 14251.
- [27] G. Kresse, D. Joubert, *Phys. Rev. B* **1999**, *59*, 1758.
- [28] B. Hammer, L. B. Hansen, J. K. Nørskov, *Phys. Rev. B* **1999**, *59*, 7413.
- [29] J. K. Nørskov, J. Rossmeisl, A. Logadottir, L. Lindqvist, J. R. Kitchin, T. Bligaard, H. Jónsson, *J. Phys. Chem. B* **2004**, *108*, 17886.